Surfaces and Interfaces 51 (2024) 104736

Contents lists available at ScienceDirect

Surfaces and Interfaces

journal homepage: www.sciencedirect.com/journal/surfaces-and-interfaces

Surface energies control the anisotropic growth of β-Ni(OH)$_2$ nanoparticles in stirred reactors

Nick Streichhan [a,1], Damian Goonetilleke [b,1], Hongjiao Li [c,1,2], Mohammad Soleymanibrojeni [c], Paul W. Hoffrogge [a], Daniel Schneider [a,d], Britta Nestler [a,d], Wolfgang Wenzel [c,*]

[a] Institute for Applied Materials - Microstructure Modeling and Simulation (IAM-MMS), Karlsruhe Institute of Technology (KIT), Kaiserstrasse 12, 76131 Karlsruhe, Germany

[b] Battery and Electrochemistry Laboratory, Institute of Nanotechnology, Karlsruhe Institute for Technology (KIT), Hermann-von-Helmholtz-Platz 1, 76344 Eggenstein-Leopoldshafen, Germany

[c] Institute of Nanotechnology (INT), Karlsruhe Institute of Technology (KIT), Hermann-von-Helmholtz-Platz 1, 76344 Eggenstein-Leopoldshafen, Karlsruhe, Germany

[d] Institute of Digital Materials Science (IDM), Karlsruhe University of Applied Sciences, Moltkestrasse 30, 76133 Karlsruhe, Germany

ARTICLE INFO

Keywords:
Cathode active materials
pH controlled precipitation
Phase-field model
Digital twin

ABSTRACT

Nickel hydroxides are an important family of electrode materials in the field of batteries and electrochemical energy storage. Two polymorphs, α-Ni(OH)$_2$ and β-Ni(OH)$_2$ have been identified, with intermediate structures also reported. However, the synthesis of the β-phase precipitants that are ideal for electrochemical applications is not trivial. The growth and morphology of the final products can widely vary with the pH. The electrochemical performance of the β-phase is sensitive to its structure and morphology, which are also sensitive to the reaction conditions. In order to better understand the initial nucleation, growth and morphological evolution of the β-phase, we present a combined experimental and theoretical study including a multiscale phase-field model for the evolution of the morphology of β-Ni(OH)$_2$. Surface indices and energies for the phase-field modeling were obtained from density functional calculations (DFT). The developed phase-field model can reproduce the growth of β-Ni(OH)$_2$ phase in different conditions. The model shows that the basal planes of β-Ni(OH)$_2$ can grow in high pH but at the same time its growth is limited by other high energy prismatic surfaces.

1. Introduction

Batteries have an important role in modern energy infrastructure and electronic devices [1,2]. A battery consists of a cathode, anode, and an electrolyte system. The performance of a battery is determined by its components, one of which is the chemistry of the electrode that controls the working voltage of a battery. With regards to the electrodes, the main requirements for practical energy storage are reactive sites accessibility, and structural stability. As electrolyte species have to reach the reaction sites in the electrode structure, accessibility of reactive sites controls the electrochemical response of the electrode, as well as its charge density. Structural stability controls the cyclability of the electrode in secondary batteries [3]. Achieving a good performance requires the optimization of the synthesis condition of the electrode [4–6]. Nickel hydroxide [Ni(OH)$_2$] is a transition metal hydroxide that has been used as an electrode material in batteries, and is also used as a precursor for the commercial production of nickel-based lithium layered oxide cathode materials. It has been used both in micro-structured and nanostructured systems and it has been demonstrated that the morphological properties of nanostructured system are superior to micro-structured electrode, as they increase the surface to volume ratio [7,8]. Recently single nano-sheets of Ni(OH)$_2$ has shown the possibility of a second electron transfer reduction from (Ni^{+3} to Ni^{+4}), which means a twofold increase in theoretical charge storage capacity of Ni(OH)$_2$ [9].

This material has been adopted for a variety of electrical energy storage applications, such as electrodes for nickel cadmium (NiCd) or nickel metal hydride (NiMH) systems as well as a precursor material for the synthesis of Ni-rich cathode materials for Li-ion batteries [10]. Ni-(oxy)hydroxides can play a role as an intercalation host or as a redox reaction electrode. Ni(OH)$_2$ exist frequently in two phases, α-Ni(OH)$_2$ and β-Ni(OH)$_2$ [11]. α-Ni(OH)$_2$ has higher charge capacity

* Corresponding author.
E-mail address: wolfgang.wenzel@kit.edu (W. Wenzel).

[1] These authors contributed equally to this work

[2] Current address: School of Chemical Engineering, Sichuan University, Chengdu, 610065, China.

https://doi.org/10.1016/j.surfin.2024.104736
Received 28 July 2023; Received in revised form 9 June 2024; Accepted 3 July 2024
Available online 6 July 2024

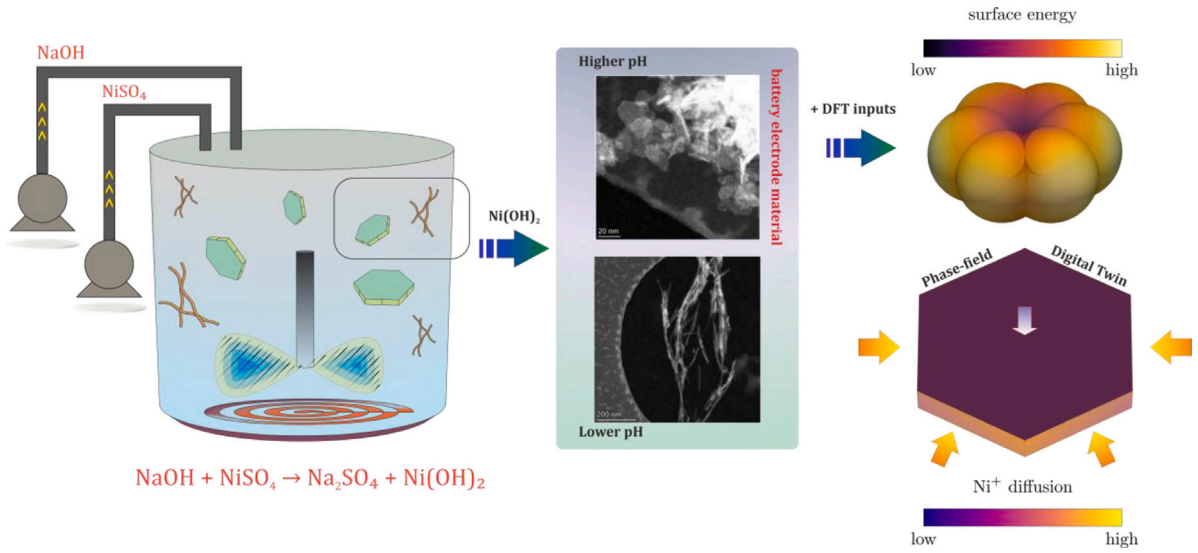

Scheme 1. Schematic illustration of theoretical and experimental studies of precursor materials.

(433 mAhg^{-1} vs. 289 mAhg^{-1}) [12], while β-Ni(OH)$_2$ is more stable and dense structure, which is ultimately better for multi-cycle electrochemical applications [13]. When adopted directly as an electrode material, α-Ni(OH)$_2$ provides a high theoretical charge capacity per gram, which after a few electrochemical cycles transforms into the more stable phase β-Ni(OH)$_2$. The morphology of Ni(OH)$_2$ depends strongly on the precipitation conditions, such as pH and concentration gradients, and the obtained morphology consequently determines the electrochemical behavior of the material [14]. For these reasons, understanding the morphology and structural evolution of Ni(OH)$_2$ is important. The relevant chemical reactions for the precipitation of Ni(OH)$_2$ and its redox reactions are given in Eqs. (1)–(4) [15,16]

$$\mathrm{Ni} + n\mathrm{H_2O} \longrightarrow [\mathrm{Ni(H_2O)_n}]^{2+} + 2\,\mathrm{e^-}, \tag{1}$$

$$\frac{1}{2}\,\mathrm{O_2} + \mathrm{H_2O} + 2\,\mathrm{e^-} \longrightarrow 2\,\mathrm{OH^-}, \tag{2}$$

$$[\mathrm{Ni(H_2O)_n}]^{2+} + 2\,\mathrm{OH^-} \longrightarrow \mathrm{Ni(OH)_2} + n\mathrm{H_2O}, \tag{3}$$

$$\mathrm{Ni(OH)_2} + \mathrm{OH^-} \longrightarrow \mathrm{NiOOH} + \mathrm{H_2O} + \mathrm{e^-}. \tag{4}$$

Previous experimental studies have investigated the morphologies and structures of the nickel hydroxide [17,18], along with theoretical efforts to determine the equilibrium shape by using DFT [19,20]. Here we extend these works with a phase-field approach, which can model a variety of physical phenomena, ranging from solidification processes [21] to grain growth [22] and micro-structure evolution at the mesoscopic scale [23]. The essence of the phase-field technique is a grand functional that incorporates all the free energies of a system in one equation. Additional driving forces, i.e. mechanical [24], chemical [25] or anisotropy formulations [26,27] can be added to model the system. Also, the link between diffusion and interface evolution can be simulated [28], which is used to study of nanostructure evolution. Using this approach we aim to study the dynamic nature of precipitation and growth of β-Ni(OH)$_2$ given an initial set of reaction conditions such as pH and concentration gradient (see Scheme 1).

2. Methods

In addition to the experiments, simulations have been performed to understand the growth of β-Ni(OH)$_2$ particles during precipitation. We first describe the experimental techniques of synthesizing and imaging β-Ni(OH)$_2$ precursors. Thereafter the multiphase-field model and the DFT calculations are explained in detail.

Synthesis and sample preparation Ni(OH)$_2$ samples were prepared by precipitation using a continuously stirred tank reactor (CSTR) setup (BASF SE, Ludwigshafen). Aqueous solutions of NiSO$_4$ and NaOH were pumped into the reactor at a rate of 15 kg/h at a controlled temperature of 25 °C, reacting to form Ni(OH)$_2$ as described in Eq. (5). The concentration of the NaOH feed solution was varied to control the pH of the reaction mixture, see Table 1. For this study, the pH values were chosen to avoid the solubility minima of Ni(OH)$_2$ from pH 8.5–12 [10]. Samples were extracted from the reaction vessel after a residence time of 30 min.

Table 1
Reaction conditions during precipitation reaction.

pH	NiSO$_4$ [mol L^{-1}]	NaOH [mol L^{-1}]
7.3	1.0	0.5
7.8	1.0	1.2
13.1	1.0	2.8
13.2	1.0	3.0

$$2\,\mathrm{NaOH} + 2\,\mathrm{NiSO_4} \longrightarrow \mathrm{Na_2SO_4} + \mathrm{Ni(OH)_2}. \tag{5}$$

X-ray diffraction X-ray diffraction (XRD) data were collected using a STOE Stadi-P diffractometer with a DECTRIS MYTHEN 1 K strip detector in Debye–Scherrer geometry. The instrument uses a Cu anode in conjunction with a monochromator which provides a wavelength of λ = 1.5406 Å. The Debye–Scherrer equation was used to estimate the average scattering domain size. The full width at half maximum (FWHM) of the (0001) reflection was chosen as the input parameter and a value of 1.84 was assumed for Scherrer's constant for the nanocrystalline layered materials [29].

Electron microscopy Transmission electron microscopy (TEM) of samples was performed on a Themis Z (ThermoFisher Scientific) double-corrected transmission electron microscope operated at acceleration voltage of 300 kV. Lift-out samples (TEM lamella) were prepared on a STRATA (FEI) dual-beam system equipped with a gallium ion source. The samples were milled at 30 kV, followed by final polishing at 2 kV to reduce the surface damage layer. Prior the milling, sample surface was protected by deposition of a carbon layer. Scanning TEM (STEM) images were collected using a high-angle annular dark-field (HAADF) detector. For statistical measurements of the electron microscopy images, the ImageJ software suite was utilized.

DFT calculations The crystal structure of β-Ni(OH)$_2$ in space group P$\bar{3}$m1 (No. 164) was utilized as the initial geometry. DFT calculations were performed with the Vienna Ab-initio Simulation Package (VASP) 5.4. To correct the overdelocalization of electrons in transition metal

oxides, the DFT+ U method was used. The Perdew–Burke–Ernzerhof (PBE) exchange–correlation functional combined with a U-J correction of 5.5 eV were employed. The wave functions were expanded in plane waves with a kinetic energy cutoff of 450 eV. Projector Augmented Wave (PAW) potentials were used to describe the interaction between the ions and electrons. Spin polarized calculations were used for all DFT calculations. A Gaussian smearing of 0.05 eV for the Fermi–Dirac distribution function was used for bulk and surface calculations. Integration in the first Brillouin zone used Monkhorst–Pack grids including $3 \times 3 \times 1$ k-points for all surfaces. Six low-index surface models of (0001), $(01\bar{1}0)$, $(10\bar{1}0)$, $(01\bar{1}1)$, $(11\bar{2}0)$ and $(11\bar{2}1)$ are created. The unit cells are a (3×3) repetition, and includes slabs of five Ni-atom layers and a minimum of 15 Å vacuum space. All the atoms in the unit cells are allowed to move freely. Geometry optimization converged until the maximum force on any free atoms was less than 0.05 eV/Å until the energy differences was below 10 meV/atom. The bulk structure of β-$Ni(OH)_2$ is firstly relaxed resulting in lattice constants of $a = b = 3.1295$ Å, $c = 4.6227$ Å, which are quite close to the experimental values of 3.122 Å and 4.642 Å respectively. The surface energy is calculated through

$$E_{\text{surface}} = \frac{E_{\text{slab}} - n_{\text{atoms}} E_{\text{bulk}}}{2A_{\text{slab}}}. \tag{6}$$

Phase-field model The phase-field method has been used extensively to understand the morphological evolution of material particles during precipitation [30–33]. The same model can be applied for understanding the kinetics and dynamics of precipitating particles from a supersaturated solution. The present phase-field model is based on the work of Nestler et al. [34] coupled with the grand-potential formulation of Choudhury et al. [35]. The multiphase-field model describes the transformation of different phases through the evolution of the phase-field parameter $\boldsymbol{\phi} = \{\phi_1, \dots, \phi_\alpha, \dots, \phi_N\}$, with N scalar phase-field variables $\phi_\alpha \in [0, 1]$. The phase-field variable changes smoothly between each grain and indicates a diffuse region with a finite width. In the case of precipitation the phase-field variable ϕ_α takes a value of $\phi_\alpha = 0$ for the liquid phase and $\phi_\alpha = 1$ for the solid precipitate. The grand potential functional is formulated as

$$\Psi(\boldsymbol{\phi}, \nabla\boldsymbol{\phi}, \mu) = \int_\Omega \left[A^{\text{cap}}(\boldsymbol{n}) \left(\varepsilon a(\boldsymbol{\phi}, \nabla\boldsymbol{\phi}) + \frac{1}{\varepsilon} w(\boldsymbol{\phi}) \right) + \psi_{\text{chem}}(\boldsymbol{\phi}, \mu) \right] \mathrm{d}\Omega, \tag{7}$$

where μ represents the diffusion potential and ε is a model parameter correlated to the interface width. $\varepsilon a(\boldsymbol{\phi}, \nabla\boldsymbol{\phi})$ and $\frac{1}{\varepsilon} w(\boldsymbol{\phi})$ represent the gradient energy density and the potential energy density, respectively and are described in detail in [34,36]. For the current two-phase system they write as $a = \gamma_0 \left| \phi_\alpha \nabla\phi_\beta - \phi_\beta \nabla\phi_\alpha \right|^2$, and $w = 16\gamma_0 \phi_\alpha \phi_\beta / \pi^2$ with the interfacial energy γ_0. The chemical contribution to the grand potential density ψ_{chem} is given as an interpolation of the individual grand potential densities ψ^α as $\psi_{\text{chem}}(\boldsymbol{\phi}, \mu) = \sum_{\alpha=1}^{N} \psi^\alpha(\mu) h_\alpha(\boldsymbol{\phi})$ with an interpolation polynomial $h_\alpha(\boldsymbol{\phi})$ described in [35]. The chemical part of the grand-potential density can be written as $\psi^\alpha(\mu) = f_\alpha(c_\alpha(\mu)) - \mu c_\alpha(\mu)$ for each phase. A parabolic expression for the free-energy densities $f_\alpha(c_\alpha(\mu)) = A_\alpha(c_\alpha(\mu) - c_{\alpha,\text{eq}})^2$ is assumed, which has a minimum at $c_{\alpha,\text{eq}}$, whose sharpness is defined by the parameter A_α. The diffusion potential is equally $\mu = \mathrm{d}f_\alpha/\mathrm{d}c_\alpha = \mathrm{d}f_\beta/\mathrm{d}c_\beta$. Accordingly, $c_\alpha(\mu) = c_{\alpha,\text{eq}} + \mu/(2A_\alpha)$ holds for any phase α. For the function $A^{\text{cap}}(\boldsymbol{n})$, the *natural formulation* [26] is used to introduce surface energy anisotropy into the system. The vector components of the normal vector $\boldsymbol{n} = \frac{\nabla\boldsymbol{\phi}}{\|\nabla\boldsymbol{\phi}\|}$ are only dependent on the phase-field gradient [26]. The evolution equations for the N phase-field variables can be written as

$$\epsilon \frac{\partial \phi_\alpha}{\partial t} = -m(\boldsymbol{\phi}, \nabla\boldsymbol{\phi}) \frac{\delta \Psi(\boldsymbol{\phi}, \nabla\boldsymbol{\phi}, \mu)}{\delta \phi_\alpha} - \Lambda, \tag{8}$$

where Λ is the Lagrange parameter to maintain the constraint $\sum_{\alpha=1}^{N} \phi_\alpha = 1$ [34]. The mobilities $m(\boldsymbol{\phi}, \nabla\boldsymbol{\phi})$ are expressed in the publications [27,37] as $m(\boldsymbol{\phi}, \nabla\boldsymbol{\phi}) = m_0 A^{\text{kin}}(\boldsymbol{n})$, where m_0 is the kinetic mobility of the α-β interface, neglecting the contribution from the anisotropy factor. The kinetic anisotropy formulation $A^{\text{kin}}(\boldsymbol{n})$ introduces anisotropy of interface kinetics into the system [37].

The composition evolves in a conservative manner

$$\frac{\partial c}{\partial t} = \nabla \cdot (M(\boldsymbol{\phi}) \nabla \mu), \tag{9}$$

where $M(\boldsymbol{\phi})$ represents the mobility of the interface, where the individual mobility for every phase is interpolated as $M(\boldsymbol{\phi}) = \sum_{\alpha=1}^{N} M_\alpha g_\alpha(\boldsymbol{\phi})$. The function $g_\alpha(\boldsymbol{\phi})$ interpolates the mobilities but is in general not the same as $h_\alpha(\boldsymbol{\phi})$ [38]. The phase mobilities can be expressed as

$$M_\alpha = D_\alpha \frac{\partial c_\alpha(\mu)}{\partial \mu} = \frac{D_\alpha}{2A_\alpha}, \tag{10}$$

where D_α are the interdiffusivities in each phase α. To simplify the implementation of the model, the evolution of the chemical potential is solved, which can be derived from the above equation (cf. [38,39]). To account for the thin-interface defect called *solute trapping* [40,41] an antitrapping current is incorporated into the evolution equation of the chemical potential, which is described in detail in [38].

When the driving forces are negligible, the equilibrium shape is governed by the minimization of interface energy. The interface energy or shape anisotropy $A^{\text{cap}}(\boldsymbol{n})$ from Eq. (7) can be expressed in the form

$$A^{\text{cap}}(\boldsymbol{n}) = \max_k \{\boldsymbol{n} \cdot \boldsymbol{\eta}_k^{\text{cap}}\}, \qquad (k = 1, \dots, N_{\text{cap}}), \tag{11}$$

The kinetic anisotropy function

$$A^{\text{kin}}(\boldsymbol{n}) = \left[1 + \delta \left(\max_k \{\boldsymbol{n} \cdot \boldsymbol{\eta}_k^{\text{kin}}\} - \max_{k-1} \{\boldsymbol{n} \cdot \boldsymbol{\eta}_k^{\text{kin}}\} \right) \right] \cdot \max_k \{\boldsymbol{n} \cdot \boldsymbol{\eta}_k^{\text{kin}}\}, \quad (k = 1, \dots, N_{\text{kin}}) \tag{12}$$

is incorporated into the system to add a variable attachment kinetic, which depends on the crystallographic direction [27]. $\boldsymbol{\eta}_k^{\text{cap}}$ and $\boldsymbol{\eta}_k^{\text{kin}}$ represent the set of N_{cap} and N_{kin} vertex vectors of the resulting surface anisotropy shape and the kinetic anisotropy shape, respectively. Here $\max_k\{\cdot\}$ returns the largest value for the scalar product and $\max_{k-1}\{\cdot\}$ the second largest value among the $N_{\text{cap/kin}}$ values. For the surface anisotropy, the vectors $\boldsymbol{\eta}_k^{\text{cap}}$ are the corners of the Wulff shape. The parameter δ is the scalar kinetic anisotropy strength parameter, which can adjust the growth rates prior to complete faceting [37].

The over-saturation within the solution is the driving force for the precursor growth. It is determined by the difference between the concentration of nickel in the solution and the equilibrium concentration of nickel $c_{\text{over}} = c_\infty - c_{\beta,\text{eq}}$. The pH value inside the CSTR dictates the equilibrium concentration of nickel. This correlation is described in [10] by Hummel and Curti. The phase-field simulations in the present work were done with periodic boundary conditions and the used parameters can be found in Appendix.

3. Results and discussion

TEM and XRD results A set of $Ni(OH)_2$ samples were prepared by precipitation reaction using a CSTR. $Ni(OH)_2$ was synthesized from the reaction of $NiSO_4$, as described in Table 1. The concentration of NaOH controls the pH of the precipitation environment and consequently the supersaturation of Ni in the solution. The regions above and below the solubility minima were chosen for sample preparation. In this study, the samples were extracted directly after reaching in the mixing nozzle, before further stirring and particle growth in the mixing chamber. $Ni(OH)_2$ initially precipitates as an amorphous α-phase, however this phase is usually not considered in industrial applications as the ordered β-phase is desired for subsequent calcination reactions. XRD data collected from the precipitated materials in Fig. 1 shows that the pH of the precipitation environment clearly determines the crystal structure of the precipitated phase. The diffraction patterns of samples prepared at pH 7.3 and 7.8 do not show distinct reflections besides a broad reflection at $2\theta \approx 10°$, which could possibly be attributed to the turbostratic α-phase. However, in the samples prepared at pH 13.1

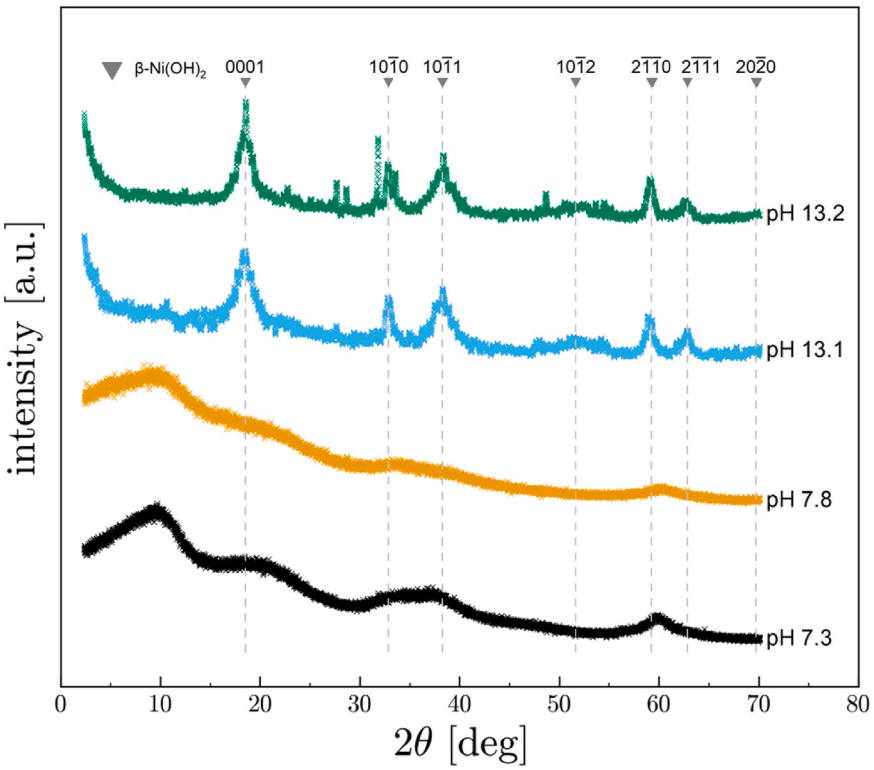

Fig. 1. X-ray diffraction data collected from $Ni(OH)_2$ samples prepared at various pH.

Table 2
Estimated particle size distribution statistics of precipitated $Ni(OH)_2$ samples as determined from TEM imaging and XRD (Debye–Scherrer).

pH	Min. area (nm^2)	Max. area (nm^2)	Average area (nm^2)	Average size (Debye–Scherrer, nm)
13.1	42.4	869.5	238.9	8.5
13.2	45.2	963.9	261.0	11.0

Table 3
The surface energies of the various β-$Ni(OH)_2$ surfaces calculated with DFT simulations.

Surface	(0001)	(01$\bar{1}$0)	(10$\bar{1}$0)	(01$\bar{1}$1)	(11$\bar{2}$0)	(11$\bar{2}$1)
$E_{surface}$ [J m^{-2}]	0.06	0.38	2.11	0.66	2.02	1.08

and 13.2, the observed reflections can be indexed to the β-$Ni(OH)_2$ structure.

TEM imaging characterizes the morphology of the precipitated particles. The morphology of the particles clearly changes by the pH during precipitation, as in Fig. 2. By looking at the electron diffraction patterns, the samples prepared at lower pH in Fig. 2a,b, have more diffuse diffraction rings compared to the well-defined rings observed in the samples prepared at pH 13.1 and 13.2 in Fig. 2c,d. This is also observed in the X-ray diffraction patterns presented in Fig. 1. Fig. 2e–h show the observed morphology of the samples precipitated at various pH. At pH 7.8, the samples appear to contain agglomerated particles which exhibit a rod-like and elongated structure. In contrast, distinct crystallites with clearly defined hexagonal shapes can be identified in the samples prepared at pH 13.1 and 13.2. The particles appear to present irregular hexagonal shapes, however this may be due to the alignment of the flat particles relatives to the detector. An estimate of the particle size distribution in these samples was also attempted using statistical measurements to determine the areas of the observed hexagonal particles, and is presented in Fig. 3. The number of particles with larger surface area increases in the sample at higher pH. This is also consistent with the average domain size estimated based on the observed XRD peak broadening and Debye–Scherrer technique, which can be compared with statistical measurements in Table 2. Both measurements indicate that the higher pH environment promotes more crystal growth.

Crystalline surface energies Based on the presented experimental results in the previous section, the basal plane of $Ni(OH)_2$ at high pH forms the hexagonal nano-plates morphology of the nanoparticles. The relaxed geometries and the surface energies of the various low-index surfaces obtained from DFT calculations are presented in Fig. 4 and Table 3. Bulk β-$Ni(OH)_2$ has a layered crystal structure and Ni is hexahedral-coordinated with OH groups. Table 3 shows that (0001) surface without the breaking of Ni-O bond has the lowest surface energies of 0.06 J m^{-2}, which is only ten to fifty percent of other surface energies. Except (0001) surface, the other surfaces have an insufficient coordination of nickel, which causes an increase of the surface energy. The results indicate that the layered structure of (0001) surface with full coordination of nickel is thermodynamically favored over the other studied surfaces. It should be noted that the surfaces presented here are clean surfaces after cleavage of the bulk structure. The surfaces except (0001) are natively positively charged and may adsorb anions from the solution to obtain surface neutralization which, could result in the termination of the crystal growth due to the burying of the binding sites.

Phase-field simulations We now use the surface energies on the relevant crystallographic surfaces to model the anisotropic shape of the β-$Ni(OH)_2$ in the phase-field simulations. For a fixed volume the shape that minimizes the total surface free energy is called the Wulff shape. The corners of the Wulff shape can be calculated by using the data in Table 3. In Fig. 5(a) we show the calculated energy plot for the surface energy anisotropy of β-$Ni(OH)_2$. The Wulff-shape is constructed as a convex hull around the energy plot [42] and is pictured from different angles in Figs. 5(b)–5(d). The Wulff shape has a hexagonal form in the *a-b* surface but is relatively thin in the *c* direction. As expected the results compares with the particle shapes found by the experimental

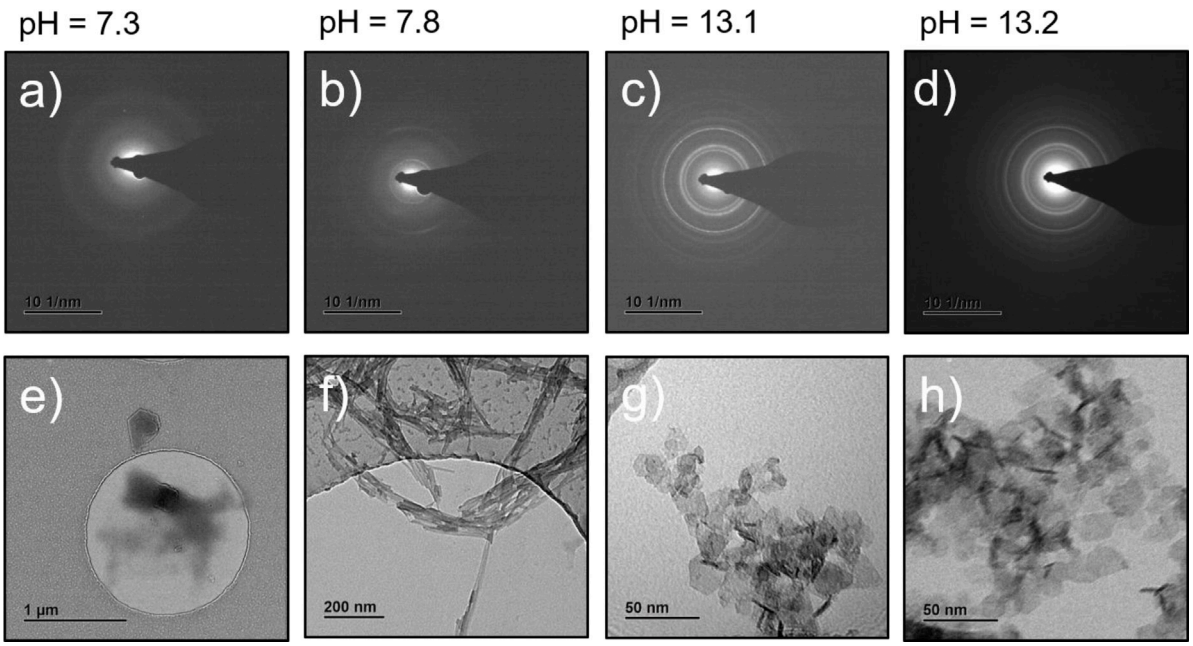

Fig. 2. (a)–(d) Electron diffraction patterns and (e)–(h) observed morphology of $Ni(OH)_2$ precipitated at various pH.

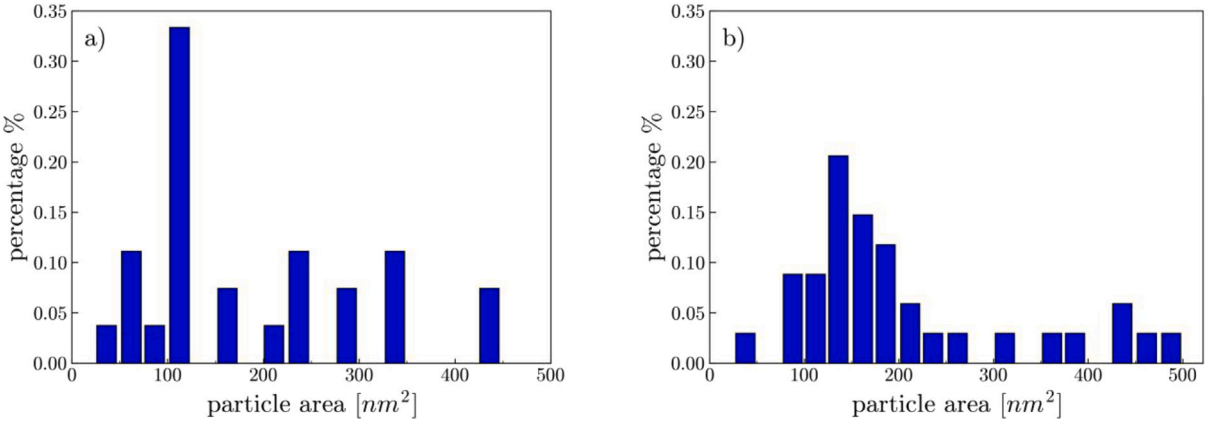

Fig. 3. Measured particle size distribution of $Ni(OH)_2$ particles observed in TEM images of samples prepared at (a) pH 13.1 and (b) pH 13.2.

precipitation of β-$Ni(OH)_2$ precursors highlighted in Fig. 2 and the atomistic geometries in Fig. 4. The equilibrium shape predicted by the Wulff construction is incorporated into the phase-field model and is shown in Fig. 5.

When reproducing the equilibrium shape of a β-$Ni(OH)_2$ precursor with the phase-field model an additional driving force that restrains the volume of the nucleus is added to Eq. (7). The *volume preservation term* was postulated by Nestler et al. [43] and is used in the phase-field model. While the reconstructed Wulff shape based on the presented phase-field model is highlighted in Figs. 6(a), 6(b) and 6(c) show the diffuse interface between the two phases in 2D and 3D respectively. Here the phase-field variable $\phi = \phi_{\text{solid}}$ is displayed where $\phi_{\text{solid}} = 1$ stands for the solid phase, here the β-$Ni(OH)_2$ phase, and $\phi_{\text{solid}} = 0$ for the solution inside the CSTR. In both views a constant diffuse interface width can be observed. The results of the simulated Wulff shape match both the theoretical equilibrium shape and the particle shapes extracted by the experimental studies in Fig. 2.

In a CSTR the precursors grow through the diffusion of Ni atoms from the over-saturated solution into the particles. We had to make several assumptions within the phase-field model to simulate the particle growth inside a CSTR. First, the reaction of the reactants is finalized when growth begins, i.e. the concentration of the solution is determined only from the inflow into the reactor. Next, the solution of the reaction products is well diluted while the stirring speed of the CSTR is constant and sufficient enough to keep the solution well mixed, i.e. the concentration is constant c_∞ far away from the nucleus. Then, the growing particles are not influenced by their neighbors and there is no interparticle collision during co-precipitation. Additionally, the convective contribution to the transport of ions into the particle arising from the fluid velocity is negligible. And finally, we only analyze the growth of β-$Ni(OH)_2$ particles which means the phase-field calculations start from a pre-existing nucleus that we put inside the simulation domain.

The evolution of particle size and shape predicted by the phase-field model can be seen at different times in Fig. 7. All simulations were carried out in a three-dimensional system with a single spherical nucleus of β-$Ni(OH)_2$ in the middle of the simulation domain, see Fig. 7(a). The transformation in shape from a spherical to a hexagonal particle and the increase in size is attributed to the connection between the surface anisotropy and the diffusion of Ni. Due to the surface anisotropy, the precipitated particle develops the expected hexagonal plate-like shape briefly after the simulation started and growth in size with ongoing time. The evolution of the Ni-concentration gradient is implied with isolines in Fig. 7, which it is also plotted in Fig. 8 for an

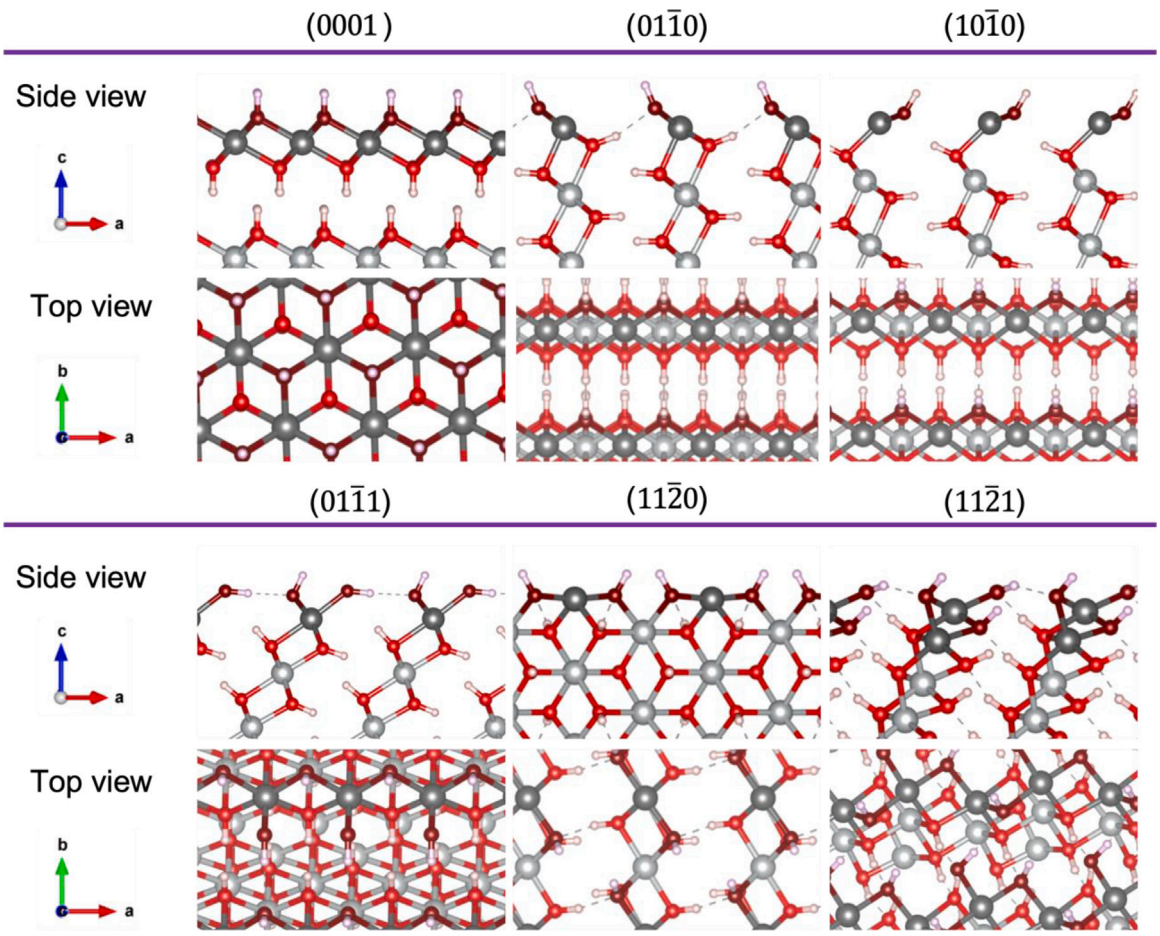

Fig. 4. The geometries of the relaxed β-Ni(OH)$_2$ surfaces. Gray: Nickel, Red: Oxygen, White: Hydrogen, Dark gray: Surface Nickel, Dark red: Surface Oxygen. (For interpretation of the references to color in this figure legend, the reader is referred to the web version of this article.)

improved illustration. Due to the symmetry of the β-Ni(OH)$_2$ system the evolution is only visualized for half of the simulation domain and specific times along the *a*- and *c*-axis respectively. The diffusion of Ni-atoms into the nucleus is highly visible along the *a*-axis. With increasing time the concentration interface between solid and liquid is migrating closer to the edge of the simulation domain, while the concentration inside the liquid matrix is decreasing. Thereby the concentration close to the particle is lower than the concentration on the domain boundary. The same can be observed along the *c*-axis - the concentration at the simulation edge decreases with advanced time but the interface shows no movement as a result of the chosen vertex vectors η_k^{kin}.

While the surface area in the *a*-*b* plane is increasing with time, it can be observed that the surface area in the *b*-*c* plane is increasing too, but the shape of the particle is only growing in the basal plane, i.e. normal to the *c*-axis. The kinetic anisotropy function in Eq. (12) is responsible for restrained growth kinetic in the *c*-direction. Observations in [44,45] show, that the thickness of β-Ni(OH)$_2$ particles is smaller than the edge length of the hexagonal shape. Therefore the vertex vectors η_k^{kin} were chosen to keep the thickness of the particle thin during the simulation. Without this kinetic adjustment all particle sides would grow with the same rate. The effect can be observed in Fig. 8. Here the velocity of the diffusive interface with a ϕ-value of 0.5 is plotted in different directions over the simulation time. It stands out, that the interface velocity in the *c*-direction converges to zero after a short adaption period, while the velocities in the *a*- and *b*-direction remain positive. It should be noted that on closer inspection the interface velocity in the *c*-direction does not converge to zero but oscillate irregularly around zero instead. This underlines the limiting effect of the kinetic anisotropy function in Eq. (12) on the particle growth, the expansion in the *c*-direction is prohibited. In contrast to that the precursor can grow unhindered in *a*-*b* plane. With increasing time the initially different interface velocities in the *a*- and *b*-direction decrease and eventually reach an equal value. With increasing particle size and decreasing Ni concentration the evolution of the precursor needs more time and energy to grow, thus the growth rate will slow down. The aspect ratio between the thickness and the diameter of the precursor underlines the result. The curve flattens over time because the interface velocity in the *c*-direction is approximately zero. The adaption period between 0 and 120u_t of simulation time is dominated by the shape transformation from an initial spherical particle to the expected β-Ni(OH)$_2$ precursor microstructure as well as relatively high interface velocities and growth rates.

4. Conclusion

In this study we have investigated the evolution of the microstructure of Ni(OH)$_2$ during precipitation and growth using a multi-scale model. The calculated surface energies from DFT calculations were used in the Wulff construction to determine the equilibrium shape of the β-Ni(OH)$_2$. The diffusion of Ni-ions was used as the driving force in the phase-field calculations and the obtained morphologies corroborated the microstructures observed in experimental data. In the phase-field model, the corners of the Wulff shape were included in the surface energy anisotropy formulation. Using an additional volume preservation term, the equilibrium shape of the precipitant was determined in 3D. The experiments confirm the precipitation of the beta phase at high pH, and DFT calculations showed the preferred growing plane of the beta

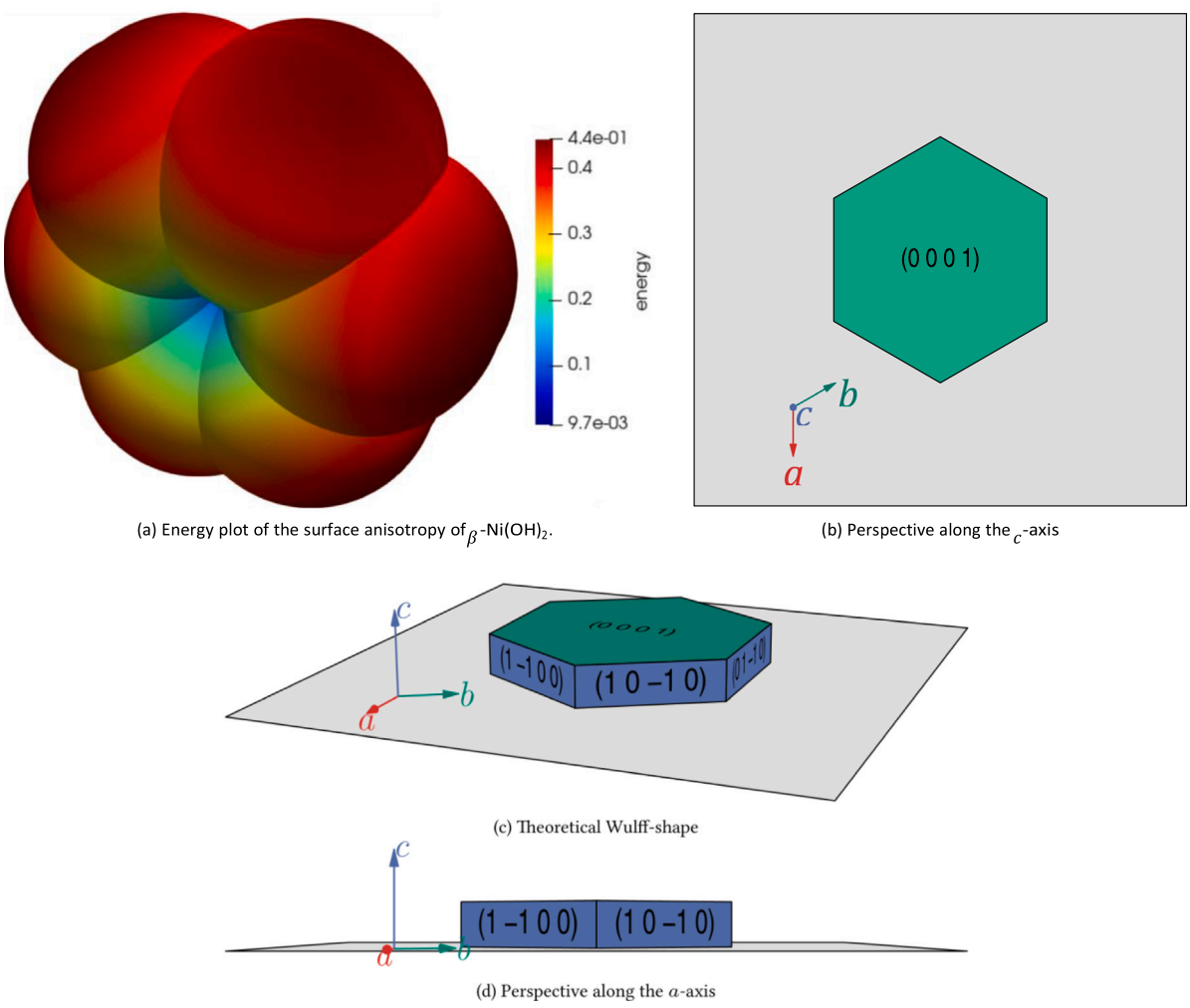

(a) Energy plot of the surface anisotropy of β-Ni(OH)$_2$.

(b) Perspective along the c-axis

(c) Theoretical Wulff-shape

(d) Perspective along the a-axis

Fig. 5. With the surface energies calculated with the DFT method and presented in Table 3 the equilibrium shape of β-Ni(OH)$_2$ can be visualized. (a) The energy plot for the surface energy anisotropy shows the min and max energies in the different crystallographic directions The Wulff shape is constructed as a convex hull around the energy plot. (b–d) The Wulff shape of β-Ni(OH)$_2$ is hexagonal in the a-b surface and thin in the b-c surface and is illustrated in different directions.

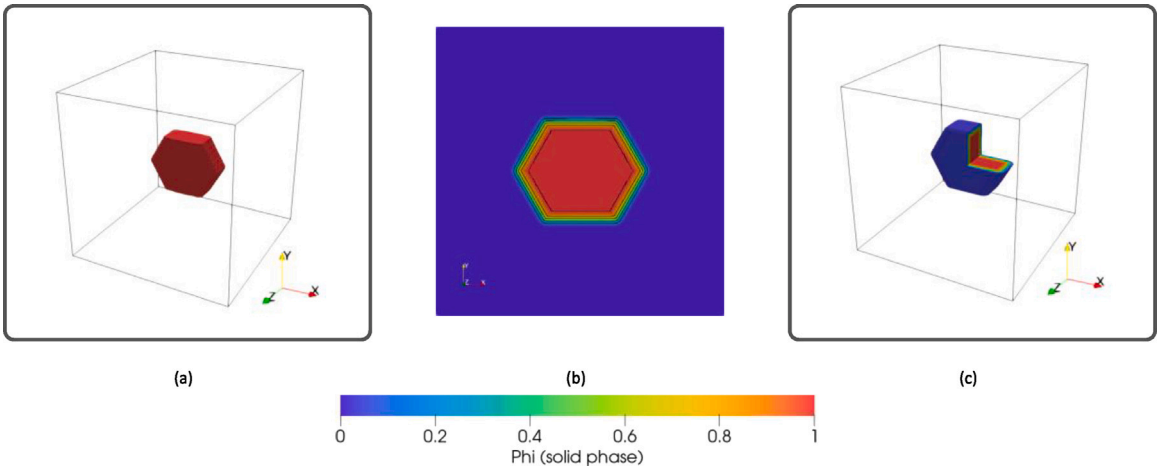

Fig. 6. Simulated Wulff shape for β-Ni(OH)$_2$ in 3D: (a) Phase-field variable $\phi = \phi_{solid}$ illustrating the 3D shape of the β-Ni(OH)$_2$ crystal in the simulation domain; (b) 2D slice in the xy plain through the particle center; (c) cut through the crystal's center visualizing the diffuse interface. Here $\phi_{solid} = 1$ marks the solid phase inside the system.

phase. By providing these inputs (static data) in our phase-field model, the model reproduces the experimental morphology and the preferred growth plane. The model additionally presents the dynamic behavior of the beta phase from precipitation to growth.

XRD and TEM characterization of precipitated Ni(OH)2 were additionally used to understand the influence of pH on the morphology of the growing particles. The α-Ni(OH)$_2$ formed during precipitation at pH values lower than 8.5, while β-phase is formed at higher pH values

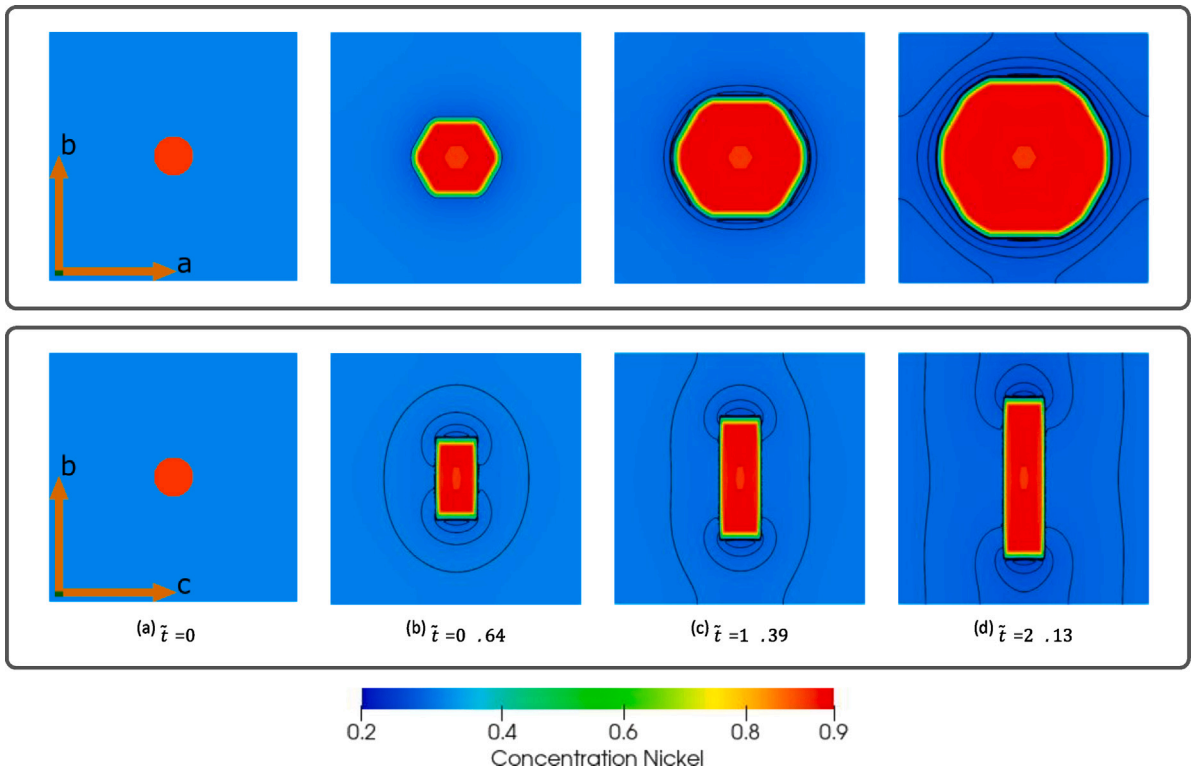

Fig. 7. Simulation of precursor growth inside a CSTR. For a better visualization of the evolution, slices at the center of the simulation domain have been cut out and are illustrated. In the top row the *a*-*b* surface is mapped while the bottom row shows the *b*-*c* surface. The concentration gradient is marked with isolines. Due to the surface energy anisotropy (Eq. (11)) the initial spherical nucleus transforms into a hexagonal plate which grows in size with ongoing simulation time. The driving force in the present simulation is the diffusion of Ni^+-atoms into the β-$Ni(OH)_2$ precursor.

of 13.1 and 13.2. The α-$Ni(OH)_2$ sample appeared to be in the form of agglomerated particles with a rod-like and elongated structure. In contrast, β-$Ni(OH)_2$ particles have 2D hexagonal shapes with different particle sizes averaging around 8–11 nm. At higher pH values, the particle sizes increase and a faster crystal growth is observed. The results of the simulations showed that the model is capable of representing the shape and growth of β-$Ni(OH)_2$. With an additional anisotropy formulation for the kinetic of different crystal surfaces, various growth rates can be modeled. This model gives us the ability to describe and predict the behavior of the β-$Ni(OH)_2$ phase within the framework of virtual material design.

CRediT authorship contribution statement

Nick Streichhan: Formal analysis, Investigation. **Damian Goonetilleke:** Formal analysis, Methodology, Visualization. **Hongjiao Li:** Data curation, Formal analysis, Investigation. **Mohammad Soleymanibrojeni:** Supervision, Visualization, Writing – original draft, Writing – review & editing. **Paul W. Hoffrogge:** Formal analysis. **Daniel Schneider:** Project administration, Supervision. **Britta Nestler:** Project administration, Supervision. **Wolfgang Wenzel:** Project administration, Supervision.

Declaration of competing interest

The authors declare that they have no known competing financial interests or personal relationships that could have appeared to influence the work reported in this paper.

Data availability

Data will be made available on request.

Acknowledgments

This research was made possible through the support of the Impuls- und Vernetzungsfonds from the Helmholtz Association, Germany, specifically under the project Digitaler Zwilling für Kathoden-Aktiv-Materialien (DigiKAM). We also extend our thanks to the Material Science and Engineering (MSE) program, also funded by the Helmholtz Association, Germany, for its contributions to our work. The authors acknowledge Lukas Metzger and Matteo Bianchini for the precipitation experiments in BASF SE, and also Matteo Bianchini and Torsten Brezesinski for valuable discussions. Additionally, we thank Andrey Mazilkin for assistance in gathering and analyzing TEM data. Furthermore the authors acknowledge the support from BASF SE, and the BIG-MAP (Battery Interface Genome-Materials Acceleration Platform), funded by the European Union's Horizon 2020 research and innovation program under grant agreement No. 957189.

Appendix. Calibration of the time scale in the simulation

The simulation parameters used in the current study are given in Table A.4 in a model-specific unit system. The real kinetic parameters related to our material system are currently unknown, such as the mobility of the interfaces and the diffusivity in the liquid. Therefore, we decided to present the results in a dimensionless manner, that allows one to fix the real time scale ones the material parameters are known. An important dimensionless parameter, that defines whether the simulation is performed in the diffusion-limiting or interface-kinetic limiting regime is the quantity

$$\tilde{D} \equiv \frac{D_{\text{liquid}}}{2mA_{\text{liquid}}\Delta c^2 R_0}, \tag{A.1}$$

where D_{liquid} is the diffusivity in the liquid, A_{liquid} is the immiscibility in the liquid, m is the mobility of the interface, $\Delta c \equiv c_{\text{solid,eq}} - c_{\text{liquid,eq}} =$

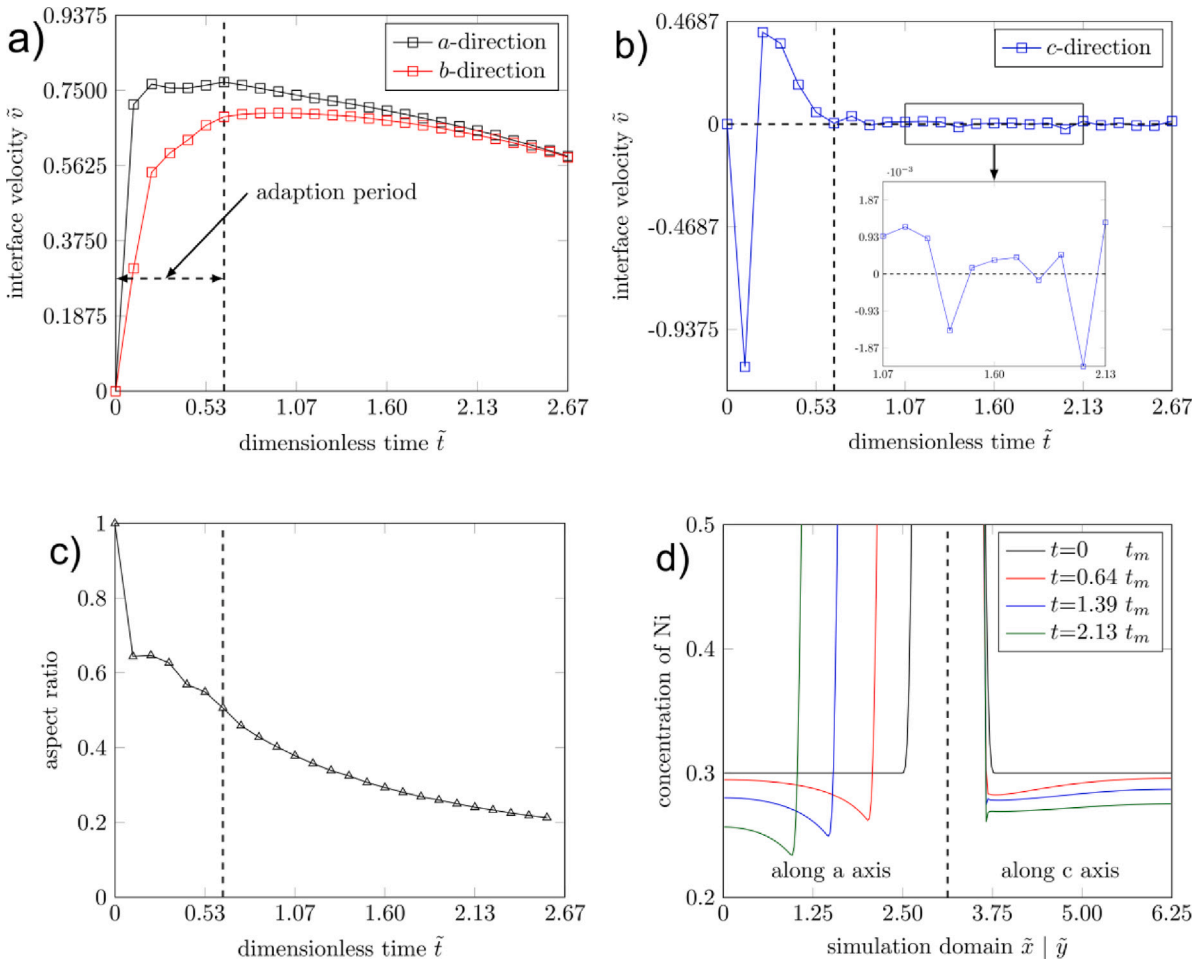

Fig. 8. Analysis of (a–b) interface velocity, (c) aspect ratio evolution and (d) concentration gradient of the simulated crystal growth. Here the aspect ratio is defined as the particle diameter per thickness. Due to the symmetry of β-Ni(OH)$_2$ the concentration gradients are shown merely for the half simulation domain.

Table A.4
Simulation parameters used in the current study. u_l is the unit of time, u_E the unit of energy and u_l the unit of length in the simulation. The grid spacing is $\Delta x = 0.5u_l$ and the timestep $\Delta t = 0.001u_t$. As an initial condition, c_∞ is used in the liquid phase for the composition field and in the solid the equilibrium composition is set.

$D_{\text{solid}}/D_{\text{liquid}}$	ϵ	m_0	γ_0	$A_{\text{solid}}/A_{\text{liquid}}$	$c_{\text{solid,eq}}/c_{\text{liquid,eq}}$	c_∞	R_0	δ
0.0/10.0 u_l^2/u_t	3 u_l	1/3 $u_l^4/(u_E u_t)$	1 u_E/u_l^2	2.0/0.5 u_E/u_l^3	0.9/0.1	0.3	$20u_l$	1

0.8 is the composition difference of solid and liquid at the interface and R_0 is the initial radius of the particle. The diffusion controlled regime belongs to $\tilde{D} \ll 1$, and the interface-kinetics (mobility) controlled regime belongs to $\tilde{D} \gg 1$. Since the mobility varies spatially due to our anisotropic treatment, firstly the value of $\tilde{D}$ is determined using the mobility prefactor m_0:

$$\tilde{D}_0 \equiv \frac{D_{\text{liquid}}}{2m_0 A_{\text{liquid}} \Delta c^2 R_0} \approx 2.34\,, \tag{A.2}$$

which shows that we are in an intermediate regime, where both the diffusivity and mobility interplay. Analyzing the two different type of facets that form, we may more precisely define two constants in either direction:

$$\tilde{D}_{\{01\bar{1}0\}} \equiv \frac{D_{\text{liquid}}}{2m_{\{01\bar{1}0\}} A_{\text{liquid}} \Delta c^2 R_0} = \frac{\tilde{D}_0}{0.38} \approx 6.17 \tag{A.3}$$

$$\tilde{D}_{\{0001\}} \equiv \frac{D_{\text{liquid}}}{2m_{\{0001\}} A_{\text{liquid}} \Delta c^2 R_0} = \frac{\tilde{D}_0}{0.00635} \approx 369\,, \tag{A.4}$$

which already shows, as wished, that the evolution of the slow facet is completely interface-kinetics controlled. The faster facet also mostly operates in the mobility controlled regime, but might show a slight coupling to the diffusion in the liquid. We therefore opt for the timescale t_m in the mobility controlled regime which is expressed as

$$t_m \equiv \frac{R_0}{4m_0 A_{\text{liquid}} \Delta c \left(c_\infty - c_{\text{liquid, eq}}\right)} \approx 187.5u_t\,, \tag{A.5}$$

where u_t is the unit time in the simulation. This timescale is used as the dimensionless simulation time. Therefore, the following non-dimensional time

$$\tilde{t} \equiv \frac{t}{t_m} \tag{A.6}$$

and dimensionless interface velocity

$$\tilde{v} \equiv \frac{vt_m}{R_0} \tag{A.7}$$

are defined. The dimensionless coordinates are written as

$$\tilde{x} \equiv \frac{x}{R_0} \tag{A.8}$$

$$\tilde{y} \equiv \frac{y}{R_0}\,. \tag{A.9}$$

References

[1] S. Brandi, A. Gallo, A. Capozzoli, A predictive and adaptive control strategy to optimize the management of integrated energy systems in buildings, Energy Rep. 8 (2022) 1550–1567.

[2] W. Wang, B. Yuan, Q. Sun, R. Wennersten, Application of energy storage in integrated energy systems — A solution to fluctuation and uncertainty of renewable energy, J. Energy Storage 52 (2022) 104812.

[3] B. He, Q. Zhang, Z. Pan, L. Li, C. Li, Y. Ling, Z. Wang, M. Chen, Z. Wang, Y. Yao, Q. Li, L. Sun, J. Wang, L. Wei, Freestanding metal–organic frameworks and their derivatives: An emerging platform for electrochemical energy storage and conversion, Chem. Rev. 122 (11) (2022) 10087–10125.

[4] G. Fiori, F. Bonaccorso, G. Iannaccone, T. Palacios, D. Neumaier, A. Seabaugh, S.K. Banerjee, L. Colombo, Electronics based on two-dimensional materials, Nature Nanotechnol. 9 (10) (2014) 768–779.

[5] P. Miró, M. Audiffred, T. Heine, An atlas of two-dimensional materials, Chem. Soc. Rev. 43 (18) (2014) 6537–6554.

[6] Gunasekaran Manibalan, Yoganandan Govindaraj, Johnbosco Yesuraj, Parasuraman Kuppusami, Govindhasamy Murugadoss, Ramaswamy Murugavel, Manavalan Rajesh Kumar, Facile synthesis of NiO@Ni(OH)2-α-MoO3 nanocomposite for enhanced solid-state symmetric supercapacitor application, J. Colloid Interface Sci. 585 (2021) 505–518.

[7] M.B.J.G. Freitas, Nickel hydroxide powder for NiOOH/Ni(OH)2 electrodes of the alkaline batteries, J. Power Sources 93 (1) (2001) 163–173.

[8] A. Caballero, L. Hernán, J. Morales, S. Cabanas-Polo, B. Ferrari, A.J. Sanchez-Herencia, J. Canales-Vázquez, Electrochemical properties of ultrasonically prepared Ni(OH)2 nanosheets in lithium cells, J. Power Sources 238 (2013) 366–371.

[9] J. Kang, Y. Xue, J. Yang, Q. Hu, Q. Zhang, L. Gu, A. Selloni, L.-M. Liu, L. Guo, Realizing two-electron transfer in Ni(OH)2 nanosheets for energy storage, J. Am. Chem. Soc. 144 (20) (2022) 8969–8976.

[10] W. Hummel, E. Curti, Nickel aqueous speciation and solubility at ambient conditions: A thermodynamic elegy, Monatsh. Chem. - Chem. Mon. 134 (7) (2003) 941–973.

[11] D.S. Hall, D.J. Lockwood, C. Bock, B.R. MacDougall, Nickel hydroxides and related materials: a review of their structures, synthesis and properties, Proc. R. Soc. A 471 (2174) (2015-02) 20140792.

[12] M.A. Kiani, M.F. Mousavi, S. Ghasemi, Size effect investigation on battery performance: Comparison between micro- and nano-particles of β-Ni(OH)2 as nickel battery cathode material, J. Power Sources 195 (17) (2010) 5794–5800.

[13] O. Guiader, P. Bernard, Understanding of Ni(OH)2/NiOOH irreversible phase transformations: Ni2O3H impact on alkaline batteries, J. Electrochem. Soc. 165 (2) (2018) A396.

[14] W. Huang, L. Ge, Y. Chen, X. Lai, J. Peng, J. Tu, Y. Cao, X. Li, Ni (OH) 2/NiO nanosheet with opulent active sites for high-performance glucose biosensor, Sensors Actuators B 248 (2017) 169–177.

[15] B. Li, H. Cao, J. Shao, H. Zheng, Y. Lu, J. Yin, M. Qu, Improved performances of β-Ni(OH)2 @ reduced-graphene-oxide in Ni-MH and Li-ion batteries, Chem. Commun. 47 (11) (2011) 3159–3161.

[16] S. Ni, X. Lv, T. Li, X. Yang, L. Zhang, The investigation of Ni (OH) 2/Ni as anodes for high performance Li-ion batteries, J. Mater. Chem. A 1 (5) (2013) 1544–1547.

[17] H. Dong, G.M. Koenig, A review on synthesis and engineering of crystal precursors produced via coprecipitation for multicomponent lithium-ion battery cathode materials, CrystEngComm 22 (9) (2020) 1514–1530.

[18] G.M. Koenig Jr., I. Belharouak, H. Deng, Y.-K. Sun, K. Amine, Composition-tailored synthesis of gradient transition metal precursor particles for lithium-ion battery cathode materials, Chem. Mater. 23 (7) (2011) 1954–1963.

[19] J.C. Garcia, J. Bareño, J. Yan, G. Chen, A. Hauser, J.R. Croy, H. Iddir, Surface structure, morphology, and stability of Li (Ni1/3Mn1/3Co1/3) O2 cathode material, J. Phys. Chem. C 121 (15) (2017) 8290–8299.

[20] J. Zhu, G. Chen, Single-crystal based studies for correlating the properties and high-voltage performance of Li [Ni x Mn y Co 1- x- y] O2 cathodes, J. Mater. Chem. A 7 (10) (2019) 5463–5474.

[21] I. Steinbach, Phase-field models in materials science, Model. Simul. Mater. Sci. Eng. 17 (7) (2009) 073001.

[22] L.-Q. Chen, Phase-field models for microstructure evolution, Annu. Rev. Mater. Sci. 32 (1) (2002) 113–140.

[23] I. Steinbach, Phase-field model for microstructure evolution at the mesoscopic scale, Annu. Rev. Mater. Res. 43 (2013) 89–107.

[24] E. Schoof, D. Schneider, N. Streichhan, T. Mittnacht, M. Selzer, B. Nestler, Multiphase-field modeling of martensitic phase transformation in a dual-phase microstructure, Int. J. Solids Struct. 134 (2018) 181–194.

[25] S. Daubner, P.G.K. Amos, E. Schoof, J. Santoki, D. Schneider, B. Nestler, Multiphase-field modeling of spinodal decomposition during intercalation in an Allen-Cahn framework, Phys. Rev. Mater. 5 (3) (2021) 035406.

[26] O. Tschukin, A. Silberzahn, M. Selzer, P.G.K. Amos, D. Schneider, B. Nestler, Concepts of modeling surface energy anisotropy in phase-field approaches, Geotherm. Energy 5 (1) (2017) 1–21.

[27] F. Wendler, A. Okamoto, P. Blum, Phase-field modeling of epitaxial growth of polycrystalline quartz veins in hydrothermal experiments, Geofluids 16 (2) (2016) 211–230.

[28] B. Nestler, A. Choudhury, Phase-field modeling of multi-component systems, Curr. Opin. Solid State Mater. Sci. 15 (3) (2011) 93–105.

[29] R. Makiura, O. Konovalov, Interfacial growth of large-area single-layer metal-organic framework nanosheets, Sci. Rep. 3 (1) (2013) 1–8.

[30] Z. Xu, P. Meakin, Phase-field modeling of solute precipitation and dissolution, J. Chem. Phys. 129 (1) (2008) 014705.

[31] T. Kitashima, H. Harada, A new phase-field method for simulating γ precipitation in multicomponent nickel-base superalloys, Acta Mater. 57 (6) (2009) 2020–2028.

[32] K. Kim, A. Roy, M.P. Gururajan, C. Wolverton, P.W. Voorhees, First-principles/Phase-field modeling of θ precipitation in Al-Cu alloys, Acta Mater. 140 (2017) 344–354.

[33] J. Zhu, T. Zhang, Y. Yang, C.T. Liu, Phase field study of the copper precipitation in Fe-Cu alloy, Acta Mater. 166 (2019) 560–571.

[34] B. Nestler, H. Garcke, B. Stinner, Multicomponent alloy solidification: phase-field modeling and simulations, Phys. Rev. E 71 (4) (2005) 041609.

[35] A. Choudhury, M. Kellner, B. Nestler, A method for coupling the phase-field model based on a grand-potential formalism to thermodynamic databases, Curr. Opin. Solid State Mater. Sci. 19 (5) (2015) 287–300.

[36] B. Stinner, B. Nestler, H. Garcke, A diffuse interface model for alloys with multiple components and phases, SIAM J. Appl. Math. 64 (3) (2004) 775–799.

[37] N. Prajapati, A. Abad Gonzalez, M. Selzer, B. Nestler, B. Busch, C. Hilgers, Quartz cementation in polycrystalline sandstone: Insights from phase-field simulations, J. Geophys. Res.: Solid Earth 125 (2) (2020) e2019JB019137.

[38] A. Choudhury, B. Nestler, Grand-potential formulation for multicomponent phase transformations combined with thin-interface asymptotics of the double-obstacle potential, Phys. Rev. E 85 (2) (2012) 021602.

[39] M. Plapp, Unified derivation of phase-field models for alloy solidification from a grand-potential functional, Phys. Rev. E 84 (3) (2011) 031601.

[40] R.F. Almgren, Second-order phase field asymptotics for unequal conductivities, SIAM J. Appl. Math. 59 (6) (1999) 2086–2107.

[41] A. Karma, Phase-field formulation for quantitative modeling of alloy solidification, Phys. Rev. Lett. 87 (11) (2001) 115701.

[42] A.R. Roosen, R.P. McCormack, W.C. Carter, Wulffman: A tool for the calculation and display of crystal shapes, Comput. Mater. Sci. 11 (1) (1998) 16–26.

[43] B. Nestler, F. Wendler, M. Selzer, B. Stinner, H. Garcke, Phase-field model for multiphase systems with preserved volume fractions, Phys. Rev. E 78 (1) (2008) 011604.

[44] H. Jiang, T. Zhao, C. Li, J. Ma, Hierarchical self-assembly of ultrathin nickel hydroxide nanoflakes for high-performance supercapacitors, J. Mater. Chem. 21 (11) (2011) 3818–3823.

[45] M.M.K. Motlagh, A.A. Youzbashi, L. Sabaghzadeh, Synthesis and characterization of Nickel hydroxide/oxide nanoparticles by the complexation-precipitation method, Int. J. Phys. Sci. 6 (6) (2011) 1471–1476.